J. Fluid Mech. (2004), *vol.* 508, *pp.* 241–264. © 2004 Cambridge University Press
DOI: 10.1017/S0022112004009176 Printed in the United Kingdom

Rotating dense currents on a slope. Part 1. Stability

By BRUCE R. SUTHERLAND, JOSHUA NAULT, KERIANNE YEWCHUK AND GORDON E. SWATERS

Department of Mathematical and Statistical Sciences, University of Alberta, Edmonton, AB, Canada T6G 2G1

(Received 28 April 2003 and in revised form 29 January 2004)

Using a novel experimental set-up, we examine the stability of an axisymmetric dense current of fluid on a sloping bottom in a rotating frame of reference. In a cylindrical tank on a rotating table, saline fluid is injected through an annular mesh encircling a cone of 1/15 slope. The resulting ring of fluid becomes unstable to periodic sinusoidal waves, whose characteristics are examined as a function of the ambient fluid depth, the rotation rate, and the salinity and depth of the dense current, the latter being related to the injection time. For experiments with relatively low-salinity currents, we find the phase speed of the instability is proportional to the rotation rate, Ω, rather than being proportional to the Nof speed, which varies as $1/\Omega$. Likewise, the number of waves observed is found to be inconsistent with existing theories for baroclinic instability of a dense current on a sloping bottom with a stationary ambient.

Surface tracers reveal that significant currents are induced in the ambient by the injection of the saline fluid and we propose that it is the coupling between the surface and bottom flow that ultimately controls the observed dynamics. In particular, we propose that barotropic instability of the surface flow controls the behaviour of the low-salinity current and, using potential vorticity conservation, we predict the phase speed of the instability should indeed be proportional to Ω. The experimental results are also compared with related work in which eddies and Ekman layers evolve from dense fluid injected from a localized source.

1. Introduction

Driven by a need to understand the propagation and stability of abyssal ocean currents, there have been numerous idealized studies examining the dynamics, in a rotating frame, of dense fluid on a slope underlying a less-dense ambient fluid. This circumstance is characteristic, for example, of the Denmark Strait Overflow (Spall & Price 1998; Jungclaus, Hauser & Käse 2001) and the Western Boundary Undercurrent which travels southward underneath the Gulf Stream (e.g. see Mellor 1996, § 7.3 and references therein).

A starting point of many theoretical and numerical studies is to assume the fluid on the slope has uniform density ρ_1 and this underlies a uniform and stationary ambient fluid of density $\rho_0 < \rho_1$. The slope fluid is further assumed to be in geostrophic balance so that it moves along the slope at constant speed C_{Nof}, the 'Nof velocity' (Nof 1983).

The stability of an infinitely long uniform current moving with this speed along a constant slope was examined by Griffiths, Killworth & Stern (1982, hereafter

referred to as GKS82). They assumed a stationary upper-layer fluid and studied long-wavelength barotropic disturbances. They showed that instability resulted from coupling between the upslope and downslope density fronts that laterally bounded the current. In particular, they showed that the current is unstable to sinusoidal waves with phase speed close to the Nof velocity.

A system of equations describing the baroclinic instability of a dense current on a slope moving with the Nof velocity under a stationary upper-layer fluid was developed by Swaters (1991, hereafter referred to as S91). His theory introduced a small perturbation parameter $\tilde{s}$, which represented the ratio of the rise of the slope over a deformation radius to the total fluid depth H, and an order-unity interaction parameter μ, which represented the ratio of the Nof velocity to the shallow-water speed based on H. He showed that for all positive μ the current was unstable provided the current depth decreased in the downslope direction over some extent of the current width. As with GKS82, the phase speed of the most unstable mode was found to be close to the Nof velocity but, unlike GKS82, the corresponding wavelength was found to be comparable to the depth and width of the current. Analysis of the energetics of the mode revealed that instability developed primarily on the downslope front of the current through baroclinic processes.

To help compare these results with laboratory experiments, Choboter & Swaters (2000) recast the equations of S91 into an axisymmetric geometry. Thus they examined the stability and evolution of a dense annular current on a conical-shaped bottom. They showed that the results agreed well with S91 even for an annular current of radius only four times the current width. The wavelength of the most unstable mode was relatively insensitive to the current width but, consistent with results expected for baroclinic instability, it was controlled primarily by the interaction parameter, μ.

No laboratory experiments have been performed that replicate the initial conditions of these theoretical models. For comparison with their theory, GKS82 presented the results of laboratory experiments in which an annular surface current overlay a dense ambient in a rotating tank with a flat bottom. The set-up precluded the possibility that the S91 baroclinic instability mechanism might occur: the speed of the geostrophically balanced current was not controlled by the body force of a dense current on a slope nor was either front of the current dynamically significant compared to the upslope or downslope fronts of the S91 current. Nonetheless, the current became unstable in all their experiments. The current itself developed after being released from between two concentric cylinders. The buoyant fluid rose, spread laterally and, through geostrophic adjustment, a horizontal shear flow developed. If the current width was smaller than approximately three times the deformation radius (based on the current depth), the current broke into a sequence of anticyclonic vortices. For larger current widths, the instability developed separately on the inner and outer fronts of the annular current. The resulting vortices grew in size through merging processes. In both cases the wavelength of the instability and the resulting vortex size was an approximately constant function of the deformation radius.

A similar result was found for sufficiently wide currents in experiments by Griffiths & Linden (1982), who studied both the unstable evolution of an annular surface current bounded on the inside by a rigid wall and the evolution of a patch of light fluid released from a cylinder. In both cases the wavelength of the instability was an approximately constant function of the deformation radius if the width of the current itself was larger than about three deformation radii. However, the unstable wavelength was found to scale as the current width if it was smaller than the deformation radius.

One purpose of this paper is to compare these results with experiments in which a dense current evolves on sloping bottom topography. In our experiments, dense fluid is injected for a finite time through a diaphanous membrane about a thin annulus on the surface of a cone. Thus we are able to observe the evolution of the dense fluid, which is dyed, and simultaneously observe the motion of the ambient inferred through the motion of surface tracers.

Our results are also compared with the dynamics of dense baroclinic eddies on a sloping bottom. Such eddies were created in experiments by Mory, Stern & Griffiths (1987) through releasing dense fluid from a cylinder in a system initially in solid body rotation. Their experiments differed from earlier experiments by Saunders (1973) in that the dense fluid initially occupied only a fraction of the total depth of the ambient. They observed that the collapsing dense patch formed a single baroclinic vortex within one rotation period and that cyclonic vorticity developed in the overlying ambient fluid. This was the result of vortex stretching in response to the initial collapse and gravitational slumping of the dense fluid down the slope. After one rotation period, the approximately geostrophically balanced eddy propagated predominately along-slope in the westward direction (corresponding to shallow fluid to the right of its motion). The westward speed of the eddy was generally found to be an order of magnitude smaller than the predicted Nof velocity. The eddy velocity also included a non-negligible northward component, the presence of which was attributed to the effects of Ekman friction.

Indeed, a significant difference between experiments with surface eddies and those with dense eddies on a rigid bottom is that an Ekman layer significantly influences the eddy evolution: it draws fluid radially away from the eddy over a thin region where viscous effects are non-negligible and can extract significant potential energy as well as kinetic energy from the eddy, leading to the spin-down and northward drift of the vortex (Mory *et al.* 1987). Similarly, a northward drift was predicted by Swaters & Flierl (1991) to occur as a result of mixing ('ventilation') of the dense eddy with the surrounding ambient.

The observation of northward-drifting eddies is not consistent in the experimental literature, however. In four sets of experiments by Whitehead *et al.* (1990), dense baroclinic eddies were generated by either injection or extraction of fluid. In each case they found the eddies coupled with cyclonic vorticity above and they propagated directly westward. The speed of the eddies was found to lie within an order of magnitude of the Nof velocity, although with considerable scatter.

The reason for this discrepancy is not well understood and has, in part, inspired a series of experiments that examine the connection between the Ekman layer, dense baroclinic eddies, and overlying ambient cyclonic vortices (Lane-Serff & Baines 1998; Etling *et al.* 2000; Cenedese *et al.* 2004).

In a series of experiments studying the continuous injection of dense fluid down slopes, Lane-Serff & Baines (1998) showed the the along-slope speed varies as a power law with a friction parameter that determines the drainage of fluid from eddies into the Ekman layer. They further show that eddies are shed regularly from the source only if the value of a vortex stretching parameter is sufficiently large.

These diagnostics will be assessed here in the context of our experiments on the instability of an axisymmetric current. The layout of this paper is as follows. The experimental set-up and analysis techniques are described in § 2. Qualitative results and their implications for analysis are given in § 3, and quantitative analyses are presented in § 4. A summary of our results are described in § 5.

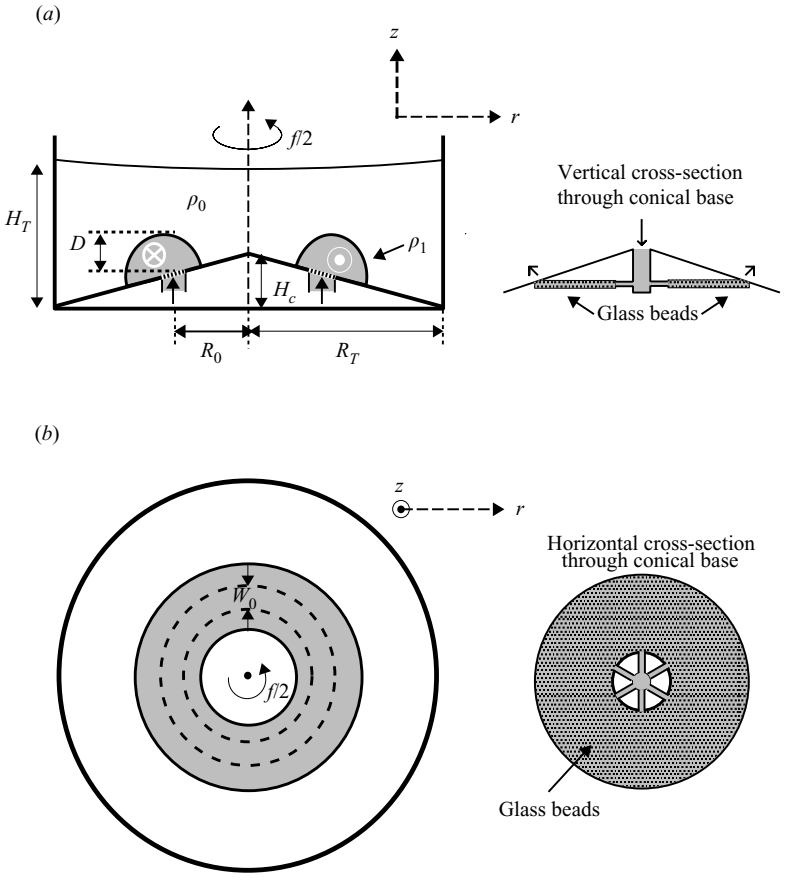

FIGURE 1. (*a*) Side view and (*b*) top view schematics (not to scale) ot tank and apparatus used to introduce an axisymmetric dense current in a rotating ambient fluid. Relevant dimensional parameters are also illustrated.

2. Experimental set-up

The experiments were performed on the Geophysical Fluids Rotating Table from Australian Scientific Instruments. The 1 m diameter table rotates at frequencies between 0.010 and 15.00 s^{-1} with better than 0.1% accuracy. A 2 m tall superstructure is fastened to the table to which cameras, lighting, and a fluid reservoir are mounted. A cylindrical acrylic tank with an inner diameter of 90.7 cm and a height of 30.0 cm was centred on the table. Conical-shaped bottom topography was fixed to the bottom of the tank. The cone had height $H_c = 3.0$ cm and radius $R_T = 45.0$ cm, as shown in figure 1.

An annulus of width $W_0 = 0.9$ cm and mean radius $R_0 = 15.0$ cm encircled the cone. It was through this annulus that fluid was injected during the course of an experiment to create a gravity current on a sloping bottom. To ensure that the fluid was injected uniformly around the ring, the fluid was injected initially into an opening at the top of the cone. Six 1 mm diameter, 5 cm long channels (the spokes of a hexagon) then carried the fluid radially outward within the cone from its centre to a cavity filled with 1 mm diameter glass beads. The beads acted to disperse the fluid evenly as it continued to spread to a radius of 15 cm. (By comparison, porous foam confined within the

cavity created irregular pathways through which the fluid would propagate.) At its outer edge the cavity underlay the annular gap. The gap was covered with a fine mesh, which acted both to prevent the emergence of glass beads through the gap and also to simulate rigid topography beneath the fluid after it had been injected through the mesh.

With the apparatus in place, the tank was filled to depth H_T with fresh water of density ρ_0. A reservoir containing a dyed salt-water solution was stationed at a height of 2 m above the bottom of the tank. When a valve was opened, this fluid was injected into the centre of the cone and ultimately upwards through the annulus.

There were four parameters that we adjusted in a range of experiments. These were the rotation rate of the table, Ω, the initial depth of the fresh water in the tank before it rotates, H_T, the density of the fluid in the reservoir, ρ_1, and the injection time T_{inj}.

Typical rotation rates ranged from $\Omega = 0.5$ to $2.0\,\mathrm{s}^{-1}$. The upper bound was set to ensure that the parabolic deflection of the free surface of the rotating fluid above the annulus did not have slope exceeding that of the bottom topography. In general, this slope is given by $r\Omega^2/g$ in which r is the radius from the axis of rotation and g is the gravitational acceleration. For $\Omega = 2\,\mathrm{s}^{-1}$, this slope is 0.061 above the annulus at $r = R_0$, which is moderately less than the slope $s = 1/15 \simeq 0.067$ of the bottom topography. Most of our analysis is performed for experiments with $\Omega \leqslant 1\,\mathrm{s}^{-1}$ so that the effects of the surface deflection can be neglected.

Typical ambient fluid depths ranged from $H_T = 5$ to 20 cm. A simple calculation shows that the resulting height of the fluid when it is in solid-body rotation is $\eta(r) = H_T + \Omega^2(2r^2 - {R_T}^2)/(4g)$. In particular, above the annulus the depth of the ambient is

$$H = H_T - 7{R_T}^2\Omega^2/(36g) - 2R_T s/3, \tag{2.1}$$

in which we have used $R_0 = R_T/3$. The last factor on the right-hand side of (2.1) represents the height of the cone above the bottom of the tank at $r = R_0$.

In experiments with moderately large density currents, we found that the injected fluid rapidly spread downslope and did not first build up into a dome-shaped current. Thus we confined our study to currents having relatively small density differences with the ambient. Specifically, in terms of $\sigma = 1000(\rho_1 - \rho_0)/\rho_0$, we studied cases with σ ranging from 0.35 to 44 with most cases examined having $\sigma = 0.71$.

The fluid was injected at an approximately constant rate for times T_{inj} between 10 and 60 s. Typical injection times are $T_{inj} = 30$ s. In some experiments the flow rate was measured using a flowmeter, and this confirmed that the flow rate was constant during the injection time. In other experiments we determined the flow rate from the change of volume of salt-water in the reservoir over the injection time. Typical flow rates are $Q \simeq 40(\pm 2)\,\mathrm{cm}^3\,\mathrm{s}^{-1}$, equivalent to a mean vertical injection speed around the annulus of $0.47\,\mathrm{cm\,s}^{-1}$.

A digital still-camera was used to take snapshots of the experiment from the side and from a top perspective angle. A grid of horizontal lines on one side of the tank was used to identify vertical distances and so measurements of the height of the dyed current could be made from the side view snapshots. For example, figure 2 shows snapshots taken in a typical experiment in which the dense current becomes unstable to 5 wavelengths around the annulus.

As well as the still-camera images, the experiments were recorded continuously in the co-rotating frame by a COHU CCD camera mounted 2 m above the table. For example, figure 3 shows successive images taken of the same experiment as in figure 2. These images were digitized and analysed using the software 'DigImage'

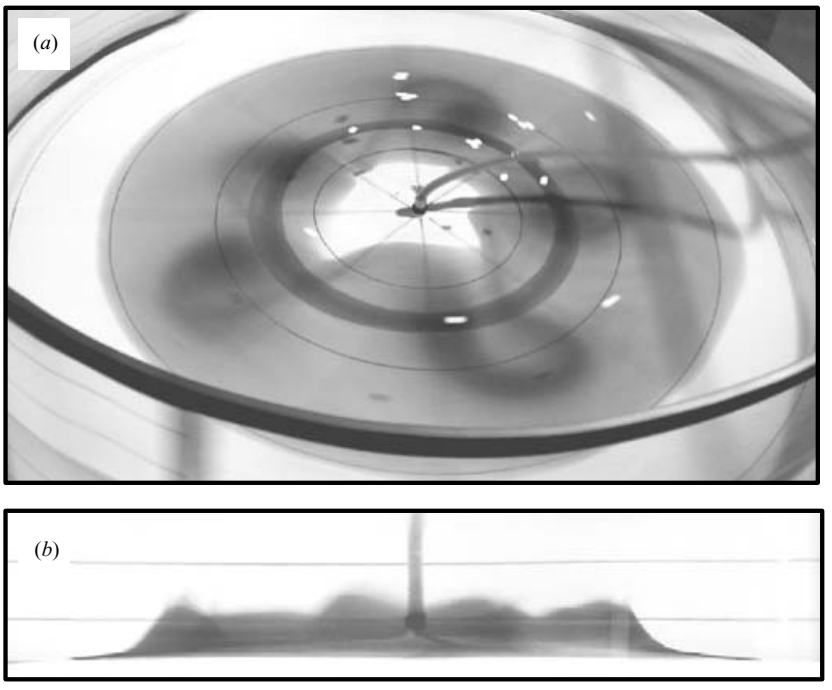

FIGURE 2. (*a*) Perspective view and (*b*) side view of an experiment in which the dyed dense current becomes unstable. The experimental parameters are $\Omega = 1.0\,\mathrm{s}^{-1}$, $H_T = 15\,\mathrm{cm}$, $\rho = 1.07$ and $T_{inj} = 30\,\mathrm{s}$. The horizontal lines in (*b*) are spaced vertically by 5 cm. The horizontal extent of the image in (*b*) has been magnified with respect to that in (*a*).

(Dalziel 1993). A grid of concentric circles spaced by 10 cm and radial lines spaced by 45° were drawn on the conical topography so that distance and velocity measurements could be taken. Thus we were able to measure the width of the current and the radial spreading rate of the Ekman layer. Surface tracers (the white specks in figure 3) were used to record the surface flow speed. Attempts to measure bottom current velocities were unrevealing: dye from potassium permanganate crystals under the current was swept away in the Ekman layer, and dye locally injected at mid-current depth resulted in non-negligible perturbations to the flow. Nonetheless, in experiments in which the current became unstable, we were able to measure the wavelength and phase speed of instabilities from perturbations of the dyed saline flow.

3. Qualitative observations

3.1. *Injection and response*

The snapshots shown in figure 4 illustrate how rotation and density differences affect the structure of the injected fluid in three characteristic experiments. In weakly rotating cases (e.g. figure 4*a*) axisymmetry is rapidly broken through three-dimensional turbulent mixing. Stronger rotation partially stabilizes the flow. If the injected fluid has the same density as the ambient (e.g. figure 4*b*) the flow evolves to form vertically coherent columnar vortices. In this case the dyed fluid extends from the bottom to the top of the ambient. If the injected fluid is even moderately more dense than the ambient (e.g. a 0.1% density difference as shown in figure 4*c*) the dyed fluid

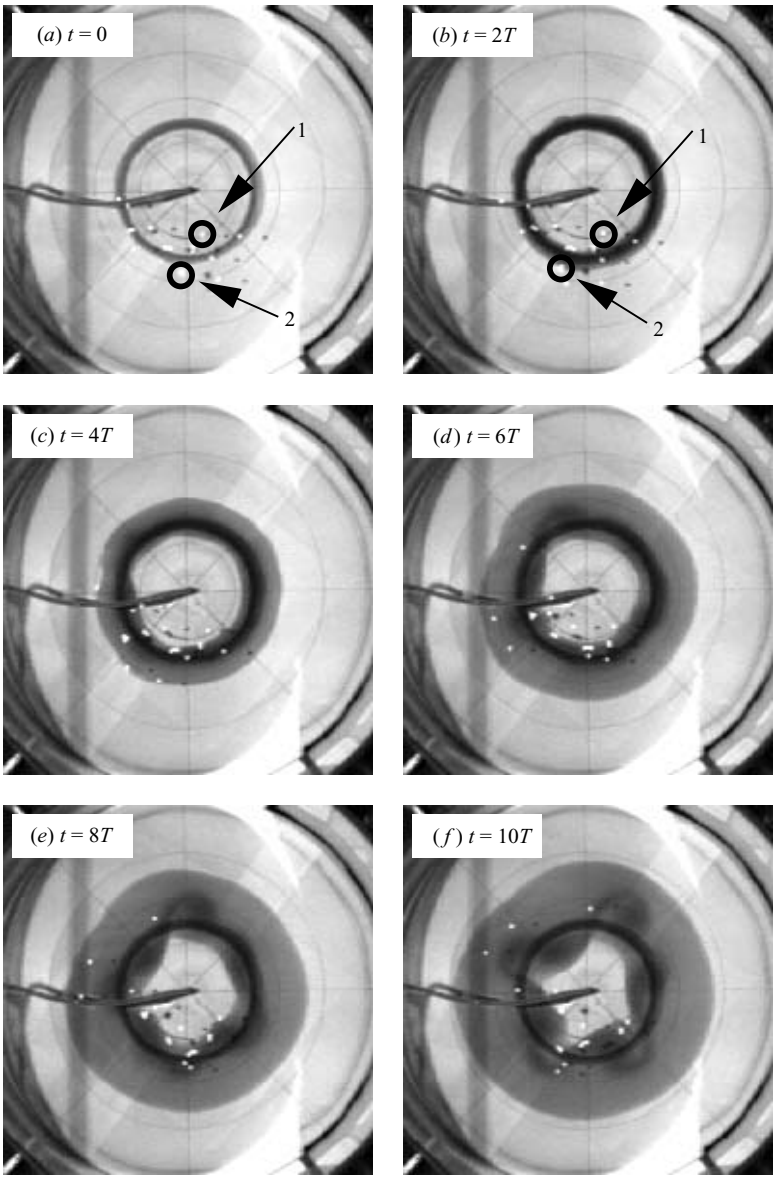

FIGURE 3. Top view of an experiment at successive times, as shown, expressed as multiples of the rotational period, $T = 2\pi/\Omega \simeq 6.28$ s. The image in (*a*) corresponds to time $t = 0$ when the fluid is first injected. Experimental parameters are the same as those given in the caption of figure 2. The particles labelled '1' and '2' (circled in black) are emphasized to illustrate the differential motion between the inside and outside of the annulus, respectively. Images are shown in the rotating frame. In the lab frame the rotation is counter-clockwise.

mixes less well with the ambient and instead evolves to form a series of isolated domes on the sloping bottom. Only the last of these characteristic cases is considered here.

Of the many experiments performed, 55 were recorded and analysed in detail. Some of these results were then rejected either because the injection through the annulus was not axisymmetric or because the density of the injected solution was so small that

(a) $\Omega = 0.1\ \mathrm{s}^{-1}$, $\Delta\rho = 0$

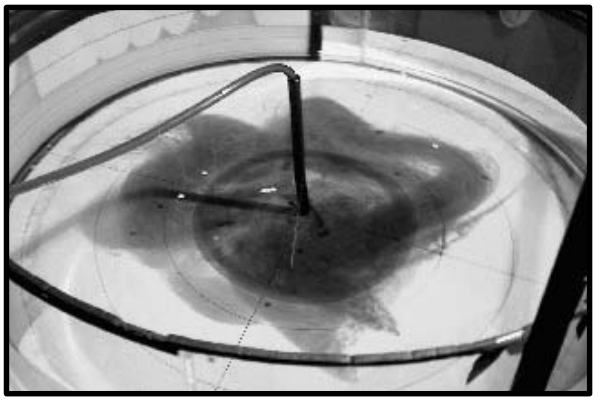

(b) $\Omega = 1.0\ \mathrm{s}^{-1}$, $\Delta\rho = 0$

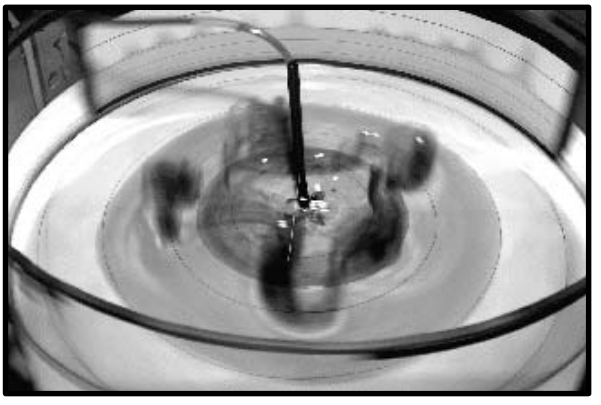

(c) $\Omega = 1.0\ \mathrm{s}^{-1}$, $\Delta\rho = 0.001\ \mathrm{g\ cm}^{-3}$

FIGURE 4. Perspective view of three experiments characterized by parameters Ω (the rotation rate) and $\Delta\rho$ (the density difference between the injected and ambient fluid), as indicated. The depth of the ambient ($H_T = 15\,\mathrm{cm}$) and the fluid injection time ($T_{inj} = 30\,\mathrm{s}$) is the same in all three cases. Snapshots are taken approximately one minute into the experiment, 30 s after fluid is no longer being injected.

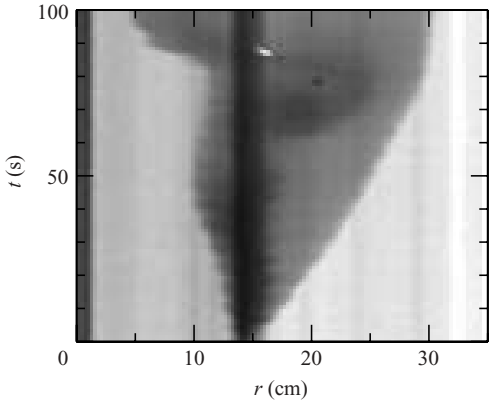

FIGURE 5. Time series taken across the radius of the tank showing the downslope spread of (weak-intensity) dye along the Ekman layer and the development of instabilities of the current (undulating dark-intensity dyed region) about $r \approx R_0 = 15\,\mathrm{cm}$. Experimental parameters are the same as those in the caption of figure 2. The position $r = 0$ corresponds to the centre of the cone and fluid is injected from the annulus at $r = R_0$ starting at $t = 0$.

turbulent jets emerged from the annulus which entrained ambient fluid and inhibited the formation of a density current. Typically the latter occurred for experiments with $\sigma \leqslant 0.35$ or with $\Omega \leqslant 0.4\,\mathrm{s}^{-1}$.

In successful experiments, the fluid emerged approximately uniformly around the annulus and assumed a dome-shaped axisymmetric structure. We did not analyse unsuccessful experiments, in which the fluid was not injected asymmetrically, for example, due to the presence of trapped air bubbles. As soon as the fluid injection begins, an axisymmetric current develops in the overlying ambient fluid. This is visualized by the motion of passive tracers on the surface. The horizontal shear associated with this flow is strongest directly over the annulus. This is illustrated in figure 3(a, b), which specifically emphasizes the motion of two tracers between a) the time when the injection first begins and b) two rotational periods later. In these images the two particles are circled and labelled '1' and '2' as indicated by the arrows. Whereas particle 1 on the inside of the annulus hardly moves, particle 2 outside the annulus moves along a circular arc by approximately 20°. In general, very little motion is observed for particles between the centre of the tank and the inside edge of the annulus, whereas the particles on the outside edge of the annulus move substantially as soon as dense fluid is injected: the ambient fluid is accelerated initially on the downslope side of the current. The resulting surface current is always anticyclonic.

3.2. *Ekman layer*

Coincident with building up the current is the development of an Ekman layer. This is apparent, for example, in figure 2(b) as the thin (approximately 1mm deep) tongue of dyed fluid moving radially in advance of the domed current. The perspective view in figure 2(a) and top views in figure 3 reveal the Ekman layer as the approximately circular region of dyed fluid with relatively weak intensity.

In most experiments, the Ekman layer initially spreads radially downslope at an almost linear rate as shown, for example by the radial time series in figure 5. At later times, when $r \gtrsim 30\,\mathrm{cm}$, the radial velocity of the front decreases moderately.

In no experiments did we observe wavy instabilities in the Ekman layer itself, as has been observed by Lane-Serff & Baines (1998); Etling *et al.* (2000), and Cenedese *et al.* (2004). This is because our experiments are run in the regime with small Froude number, based on the ratio of the observed spreading rate to the theoretical shallow water speed of the Ekman layer: $Fr_\delta \equiv C_{Ek}/(g'\delta\cos\theta)^{1/2} \ll 1$, in which $g' = g(\rho_1 - \rho_0)/\rho_0$ is the reduced gravity, θ is the angle of the slope with the horizontal, and $\delta = (2\nu/f)^{1/2}$ is the theoretical Ekman layer depth. In our experiments, the Coriolis parameter $f = 2\Omega$ and $\nu = 0.01\,\mathrm{cm^2\,s^{-1}}$ is the kinematic viscosity of water. Wavy instabilities were shown by Cenedese *et al.* (2004) to occur if $Fr_\delta \geqslant 1$.

3.3. *Characteristics of the dense current*

The injected fluid emerged from the gap in the annulus and rapidly adjusted to the ambient fluid environment forming a dome-shaped ring. As the fluid is being injected the depth of the dense fluid steadily increases and spreads radially both inward and outward from the annulus.

In general, we find that the dense fluid must build up to a critical depth before it becomes unstable to normal-mode disturbances. It would be useful to estimate this depth as a function of the volume of injected fluid. However, this is non-trivial. While the fluid is being injected, not only does it partially entrain ambient fluid (particularly in small-σ experiments) but it is partially extracted from the developing current by Ekman pumping. Hence the total volume of the current is equal to the volume injected less that extracted along the bottom boundary layer. Indeed, in experiments with large σ and small Ω we find that the radial transport of fluid along the bottom boundary layer is sufficiently large that the current does not build up to sufficient depth to become unstable.

The volume of the current is estimated from measurements of the depth D and width W of the current. Both measurements have associated with them 0.5 cm errors. The error in D reflects the variations in the depth of the fluid around the annulus even before it becomes unstable. The error in W reflects the ambiguity in discerning a specific point where the dome meets the Ekman layer.

3.4. *Instability characteristics*

In most experiments in which dense fluid is injected for a sufficiently long time (typically 30 s or more) the current becomes unstable to periodic sinusoidal waves. A clue to the dynamics of the instability is given by noting that the phase speed of the instability is the same as the surface flow speed.

For example, figure 6 shows a time series constructed by recording the light intensities over successive times extracted around a ring of radius $R_{TS} = 18\,\mathrm{cm}$, moderately wider than the mean radius of the annulus. The horizontal axis in the plot is the angle, θ, increasing in a counter-clockwise direction around the ring, with $\theta = 0$ corresponding to the right-hand extremity of the ring in images such as those shown in figure 3. Soon after the injection begins, the Ekman layer reaches this ring. This is apparent from the uniform darkening of intensities for all θ. A short time later, a periodic pattern of even darker intensity regions appears. These reflect the development of unstable spatial undulations in the dense current at $r = R_{TS}$. Their slope in the space–time plot gives the speed of propagation of the instability. The negative slope indicates that the instability progresses in a clockwise direction, opposite to the direction of rotation of the table: the instability is anticyclonic.

In most experiments, the slopes are approximately constant during the initial development of the instability and during the formation of the vortices. Significant

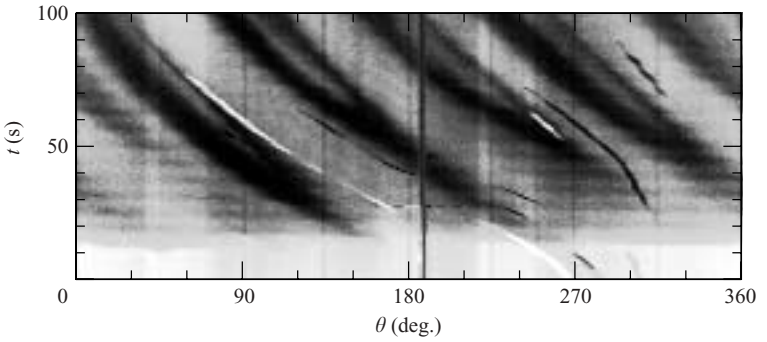

FIGURE 6. Time series determined around a circle of radius 18 cm. Experimental parameters are the same as those given in the caption of figure 2.

deceleration to speeds an order of magnitude smaller is observed at later times in experiments with relatively small upper layer depth, $H_T = 5$ cm, and relatively high rotation rates ($\Omega \geqslant 1.5$). We attribute this deceleration to vortex stretching by Ekman pumping which is significant in this parameter regime.

Also apparent in figure 6 are white streaks, which are formed by the approximately circular motion of the surface tracer particles. (The thin dark streaks are the shadows of tracers on the tank bottom.) The streaks form lines with the same slope as the underlying broad dark bands, a feature observed in all experiments in which instability develops. Thus the surface flow and, presumably, the whole vertical column of the ambient fluid moves at the same speed as the instability.

This observation, which is typical of most experiments, indicates a significant difference between the initial conditions of the experiments and those imposed in the theory of Choboter & Swaters (2000) and also, more generally, in those of S91 and GKS82. The theories assumed an initially stationary ambient layer overlying a geostrophically balanced current. In the experiments not only is the ambient flow non-stationary, but the equal surface flow speeds and unstable-mode phase speeds indicates that the ambient region significantly affects the instability dynamics.

This relationship is examined in more detail in the following section.

4. Quantitative analysis

4.1. *Ekman layer*

All experiments show the radial spreading of an Ekman layer with a depth on the order of 1 mm, comparable to the theoretical Ekman layer depth, δ. That is, the Ekman number (the ratio of the observed layer depth to δ) in this part of the flow is $Ek \simeq 1$. The spreading of the Ekman layer acts to draw fluid out of the current. The vertical velocity consequently produced by Ekman pumping is given by $w_e = \delta\xi/2$ in which ξ is the vorticity associated with the current. Although the current speed is not measured directly, using a top-hat approximation for the current structure we show in § 4.5 that the surface current speed and the phase speed of instabilities to the dense current is given approximately by $C_0 = -\Omega D R_0/H$. We take this as a characteristic measure of the flow at the edge of the dense current and, consistent with the top-hat approximation, we take W_0 as the characteristic width of the current. Thus, we estimate

$$w_e \simeq \frac{\delta C_0}{2W_0}. \tag{4.1}$$

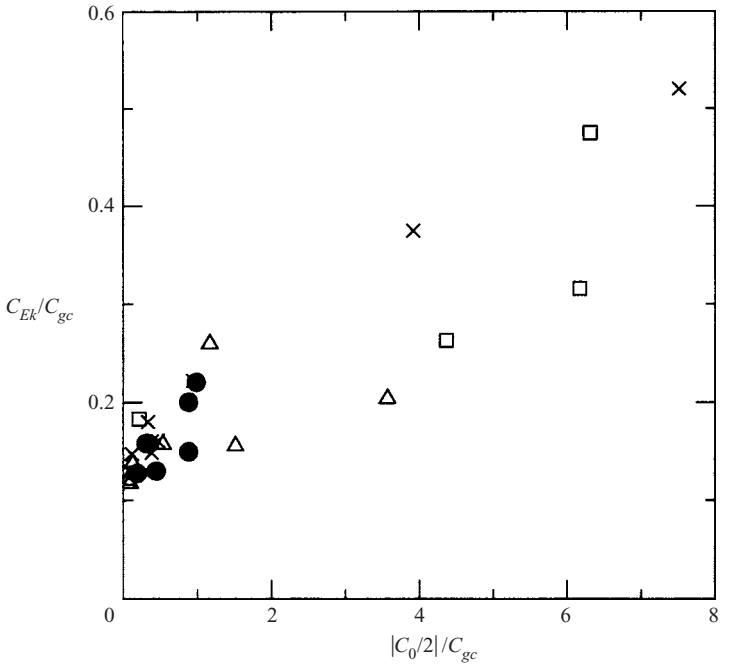

FIGURE 7. Radial spreading velocity of Ekman layer versus theoretical estimate for spreading rate. Both axes are non-dimensionalized by the shallow water speed based on the Ekman layer depth, δ. The symbols represent experiments with different rotation rates: $\Omega < 1.0\,\mathrm{s}^{-1}$, solid circle; $\Omega = 1.0\,\mathrm{s}^{-1}$, open triangles; $\Omega = 1.5\,\mathrm{s}^{-1}$, open squares; $\Omega = 2.0\,\mathrm{s}^{-1}$, crosses.

We estimate the radial spreading velocity, v_e, using conservation of mass: $2\pi R_0 \delta v_e \simeq 2\pi R_0 W_0 |w_e|$. Thus, we have

$$v_e \simeq |C_0|/2 = \frac{\Omega D R_0}{2H}. \tag{4.2}$$

Figure 7 shows a plot of the measured radial Ekman velocity, C_{Ek}, versus the predicted value given by (4.2). Both axes are normalized by the non-dimensional shallow water speed, C_{gc}, based on the Ekman layer depth. Explicitly $C_{gc} = (g'\delta\cos\phi)^{1/2}$, in which ϕ is the angle of the slope with the horizontal (e.g. see Cenedese *et al.* 2004). For clarity, we have plotted points only for experiments in which $T_{inj} = 30\,\mathrm{s}$. To avoid plotting points with large measurement errors in the values of D/H, we have also restricted which points we plot by the condition $H_T \geqslant 10\,\mathrm{cm}$.

Although there is clearly an increasing linear trend, we find C_{Ek} is not proportional to v_e: the intercept of the best-fit line through the data (not shown) occurs for $C_{Ek} \simeq 0.15 C_{gc}$, significantly away from the origin. The theory fails because, even in the absence of Ekman pumping, there would be downslope flow of the dense currents due to buoyancy effects alone. Indeed, the data near the intercept correspond to experiments with such large values of σ that $C_{gc} \gg v_e$. If viscous effects could be neglected, and given ϕ is small in our experiments so $\cos\phi \simeq 1$, we might anticipate that the radial spreading speed should be on the order of C_{gc}, which is the approximate speed of a gravity current (e.g. Benjamin 1968; Rottman & Simpson 1983). Because we observe that the Ekman number is order unity, however, viscous effects cannot be neglected. The limiting speed $C_{Ek} \simeq 0.15 C_{gc}$ is therefore a measure of the downslope

speed of a gravity current whose motion is determined by a balance of downslope pressure-gradient and viscous forces in the presence of rotation.

We note that the ordinate axis in figure 7 is just the Ekman-layer-based Froude number Fr_δ. Because $Fr_\delta < 1$ in all our experiments, we do not expect to see wavy disturbances in the Ekman layer, consistent with the observations of Cenedese *et al.* (2004).

When injection begins, the induced speed of the ambient is given approximately by C_0, which increases as the depth D of the current increases. Thus, by (4.1), the Ekman pumping velocity increases in time. By extrapolation, we define T_{Ek} to be the time at which the Ekman pumping velocity is equal and opposite to the injection velocity. In non-dimensional form we find

$$\Omega T_{Ek}/2\pi = H/(\delta\pi), \tag{4.3}$$

which in our experiments takes values between approximately 10 and 50. These values are greater than those of Mory *et al.* (1987) who based their timescale estimate on the decay time of an isolated baroclinic vortex. In experiments we find that the time for instability when it occurs is shorter than T_{Ek}. Thus, the dynamics of Ekman pumping are not expected to affect significantly the observed dynamics of the current evolution.

4.2. *Current volume*

The total volume of injected fluid is measured accurately by recording the change in volume of fluid in the reservoir before and after an experiment. The actual volume of fluid associated with the dense current is estimated from measurements of the fluid width W and maximum depth D before it becomes unstable. Both these measurements are accurate to within 1 cm. Assuming a parabolic profile for the height of the current as a function of radial distance, the volume of the current is $4\pi R_0 DW/3$.

Figure 8 plots values of the computed current volume against the injected volume for a range of experiments. For short injection times and small rotation rates, the two values agree reasonably well. However, at high rotation rates and for large injection volumes, the volume of the current is significantly less than that injected. Ekman pumping accounts for some of this discrepancy (between 100 and 400 cm^3) with the remaining difference resulting from errors in estimating the width of the current when its depth is small.

4.3. *Current width*

Just as Griffiths & Linden (1982) found the expansion of the current width to increase with the Rossby radius, so we observe an increasing trend. The measurement of width is particularly difficult in experiments with current depths less than 1 cm in which case the boundary between the current and Ekman layer is vaguely defined. Figure 9 plots the width only for those experiments with current depths $D > 1$ cm. The plot shows that the measured expansion of the current width increases approximately linearly as a function of the Rossby radius based on the lower layer depth, $L_D = (g'D)^{1/2}/f$. From these data we find $W \simeq 4.6L_D + W_0$.

Alternatively, we may compare the width of the current with the Rossby radius $L_R = (g'\bar{h})^{1/2}/f$ in which $\bar{h} = [D(H-D)]^{1/2}$. When the extent of the broadened current is plotted against L_R (not shown) we likewise observe an approximately linear trend but rescaled so that $W \simeq 3.3L_R + W_0$.

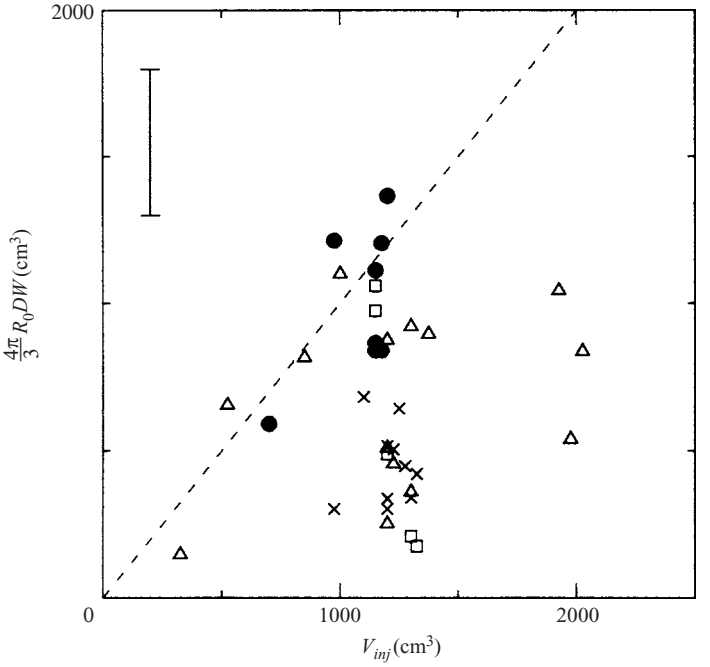

FIGURE 8. Estimated current volume versus measured input volume. Symbols represent data for experiments with different rotation rates as in figure 7. The typical error in computed current volume is indicated in the top, left-hand side of the plot. The diagonal dashed line shows where the computed volume equals the injected volume.

4.4. *Current stability*

In most experiments we observed that the current becomes unstable to a sinusoidal instability exhibiting regular undulations around the ring. The stability regimes are indicated in figure 10, which illustrates whether instability occurs as a function of the non-dimensional depth and width of the current. In general we find the current is stable (as indicated by the solid circles) either if the width is small compared with L_R or if the current depth is sufficiently small compared with H. In the latter case, the depth is so small that the current is not much deeper than the Ekman layer and so the width itself is difficult to determine accurately. Nonetheless, the stability boundary delineated by these points is consistent.

In experiments in which instability occurs the current breaks into unstable modes with wavenumbers, N_λ, typically between 4 and 6, as indicated by the different symbols in figure 10.

4.5. *Characteristics of unstable modes*

For comparison with the experiments by Griffiths & Linden (1982), in figure 11 we plot the observed wavelength $\lambda = 2\pi R_0/N_\lambda$ versus the width of the annulus, W_0 for experiments in which instability occurs. The different symbols plotted in the figure indicate the corresponding rotation rate. A vertical line is drawn in cases where N_λ could not be clearly identified as a single integer and symbols are plotted at either extreme of the line corresponding to wavelengths determined from bounding values of N_λ. Both axes are plotted in non-dimensional units with respect to the Rossby deformation radius L_R.

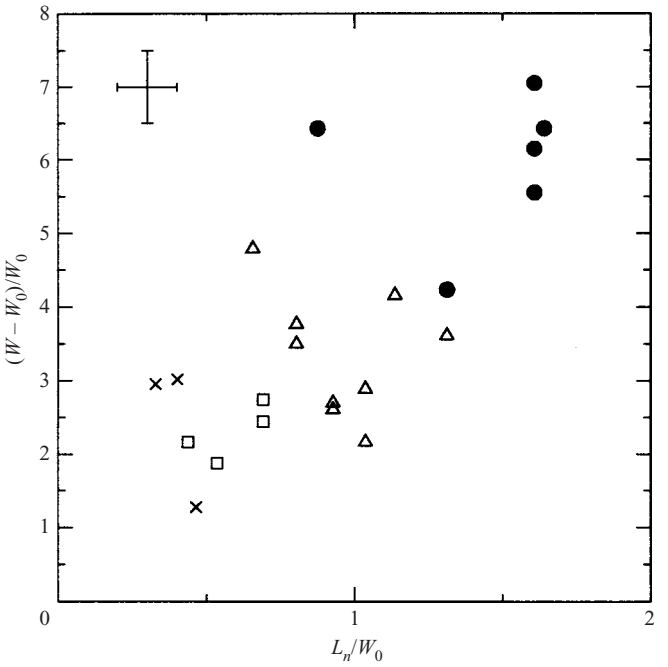

FIGURE 9. Current width as a function of the Rossby deformation radius, L_D, based on the current depth, D. Both are non-dimensionalized by the annulus gap width, W_0. Symbols plotted indicate rotation rate, as in figure 7. Typical error bars are indicated in the upper left-hand corner of the plot.

The figure shows a linear trend with mean slope 21.7. Because W_0 is constant in all experiments, the plot shows that when instability occurs the wavelength is relatively insensitive to the rotation rate, density difference between the current and ambient, depth of fluid in the tank and depth of the current itself.

In contrast, the inset to figure 11 plots the non-dimensional wavelength against the width of the current measured after it is injected but before it becomes unstable. In this case there is no clear linear trend.

It would be incorrect on the basis of these results to conclude that the wavelength should always be approximately constant. We have performed experiments only in the case $W_0 < L_R$. In the regime where the width of the source is larger than L_R, we expect the wavelength should be set by L_R rather than W_0 as observed in experiments by Griffiths & Linden (1982) and GKS82. Our experimental design does not permit us to examine this hypothesis at present.

The angular phase speed C is measured from the circular time series plots, such as that shown in figure 6. C is found from the mean slopes of the edges of the dark regions shortly after they appear (typically over the first 30 s of an experiment). We find this speed is indicative both of the phase speed of the initial mode and also, typically, of the eddies that ultimately develop. C is also identical to the angular speed of the surface tracers. The exception occurs for experiments with fast rotation rates and small ambient fluid depths in which case Ekman pumping induces significant vortex stretching in the upper layer which decelerates the surface flow and eddies after approximately 30 s.

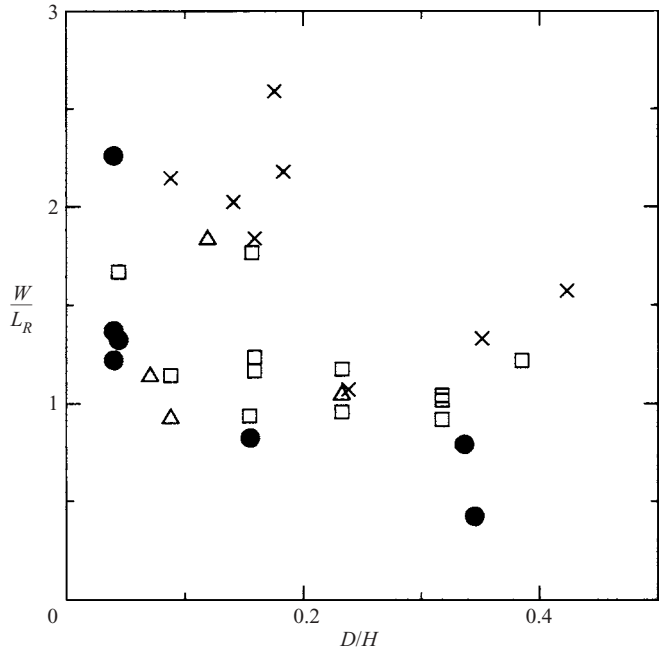

FIGURE 10. Regime diagram showing stability of current as a function of non-dimensional current width and depth. Solid circles indicate experiments in which the current remains stable. Other symbols are drawn for experiments in which the flow becomes unstable to a mode with wavenumber 4 (open triangles), wavenumber 5 (open squares) and wavenumber 6 (crosses).

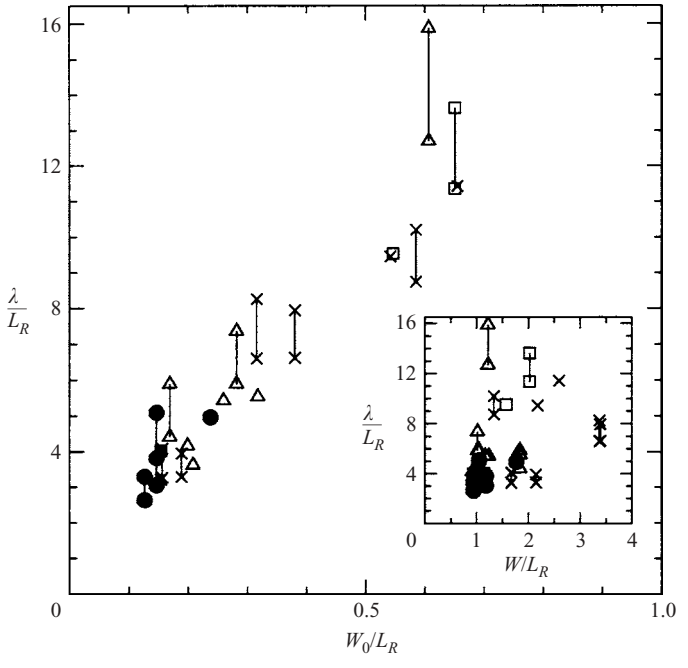

FIGURE 11. Wavelength of the instability versus current width. Both are non-dimensionalized by L_R. Symbols correspond to values of the rotation rate, as in figure 7.

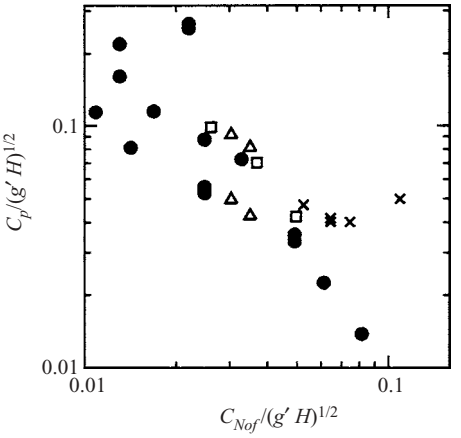

FIGURE 12. Phase speed of the unstable modes versus Nof speed, with both axes non-dimensionalized by $(g'H)^{1/2}$. Different symbols are plotted depending on the relative density of the injected fluid: solid circles for $\sigma \leqslant 8$, open triangles for $8 < \sigma \leqslant 16$, open squares for $16 < \sigma \leqslant 64$, and crosses for $\sigma > 64$.

To compare the speed of the observed disturbances with theories that predict linear speeds, we construct the linear phase speed C_p from the measured angular phase speed C via $C_p = R_{TS}C$, in which $R_{TS} = 18\,\text{cm}$ is the radius at which we construct the circular time series. This conversion from radians to distance per unit time is somewhat arbitrary: the angular phase speed would be approximately the same at $R_0 = 15\,\text{cm}$ but the (linear) phase speed would be less. Despite this ambiguity, C_p can be taken as a measure of the linear speed accurate to within a constant of order unity. The value of the proportionality constant does not affect our conclusions based on the observed trends.

The theoretical steady-state along-slope speed of a geostrophically balanced dense fluid underlying a stationary ambient is given by the 'Nof velocity' (Nof 1983), $C_{Nof} = sg'/f$, whose value is a consequence of a balance between buoyancy, Coriolis and body forces. A simple derivation is provided in the Appendix.

If indeed the observed instabilities occur due to perturbations of a geostrophically balanced dense current on a slope underlying stationary fluid, then we would expect $C_p \simeq C_{Nof}$. However, figure 12 shows there is an inverse rather than direct proportionality relationship between C_p and C_{Nof}.

This figure plots different symbols corresponding to the relative density differences in the experiments as characterized by σ. The plot indicates that the phase speed of instabilities developing on low-density currents decreases with C_{Nof}, whereas the phase speed is approximately independent of C_{Nof} for large-density currents (with $\sigma > 64$).

The axes in this plot are normalized with respect to the shallow water speed, $C_H = (g'H)^{1/2}$, based on the total fluid depth H. Thus, the abscissa C_{Nof}/C_H is equivalent to the slope parameter $\tilde{s}$ used by S91 and Choboter & Swaters (2000). In their asymptotic theory, $\tilde{s}$ must be much smaller than unity. The plot therefore shows that the experimental parameters lie within this asymptotic regime, i.e. $\tilde{s} \lesssim O(0.1)$, and also within the regime of observed cold pools in the ocean such as the mid-Atlantic Bight (Houghton *et al.* 1982).

Though not shown, we have also computed the Rossby number $Ro = U/(fR_0)$, which measures the relative importance of the centripetal force and the Coriolis

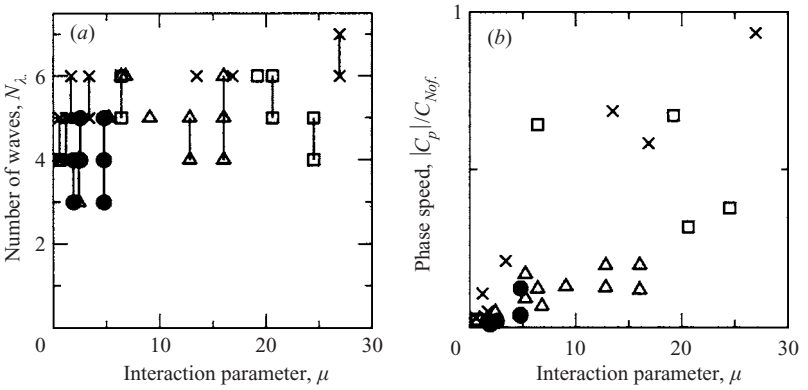

FIGURE 13. (*a*) Number of waves of instability and (*b*) non-dimensional phase speed both plotted as functions of the interaction parameter μ, which measures the relative importance of baroclinicity for destabilization of the current. In both diagrams, symbols correspond to values of the rotation rate, as in figure 7.

force. In all experiments, we find $0.01 < Ro < 0.05$, well within the regime required for geostrophic balance to occur.

To draw further contrasts between our results and those predicted by Choboter & Swaters (2000), we examine how the number of waves of instability and the relative phase speed varies with the S91 'interaction parameter' $\mu = D/(H\tilde{s})$. This is a measure of the destabilizing effect of baroclinicity relative to the stabilizing effect of the beta-plane slope. In their theory, μ must be of order unity. Nonetheless they extrapolate their results to large μ.

Assuming a stationary upper layer, Choboter & Swaters (2000) predict that the flow is unstable for all μ and that N_λ increases with μ. For example, they find N_λ increases from 5 when $\mu = 1$ to 15 when $\mu = 10$. As shown in figure 13(*a*), and consistent with figure 11, we find that the observed wavenumber does not vary significantly with μ. Possibly there exists a weakly increasing trend, but the data are too scattered to draw any definitive conclusions.

The phase speed predicted by Choboter & Swaters (2000) also differs. They predict that the ratio of the phase speed to Nof speed should be approximately unity for a wide range of interaction parameters. However, as shown in figure 13(*b*), we find that the phase speed is an order of magnitude smaller than the Nof velocity for small μ. For large μ the relative phase speed varies between 0.1 and 1.

A clue to the reason for the discrepancy is given by the motion of surface tracers. We find that the surface flow begins to move as soon as the dense fluid is injected from the annulus. Typically, a small radial component to the velocity is apparent in the first ten seconds as the dense fluid is first injected from the annulus. Though this component of the velocity is not measured directly it can be seen by digitally tracking particle streaks. As a result some particles move outward to the ring at $R_{TS} = 18$ cm where the circular time series is extracted. Particles that reach this ring after the first 10 s typically remain on this ring for long times, between 10 and 30 s. Thus the radial component of the surface flow is negligibly small after the initial transient time. The azimuthal flow that develops is anticyclonic and, in experiments in which current becomes unstable, the flow speed is comparable to the phase speed of the instability observed in the underlying fluid. Indeed the two speeds are the same when the surface particle directly overlies a dense eddy as expected for the dynamics

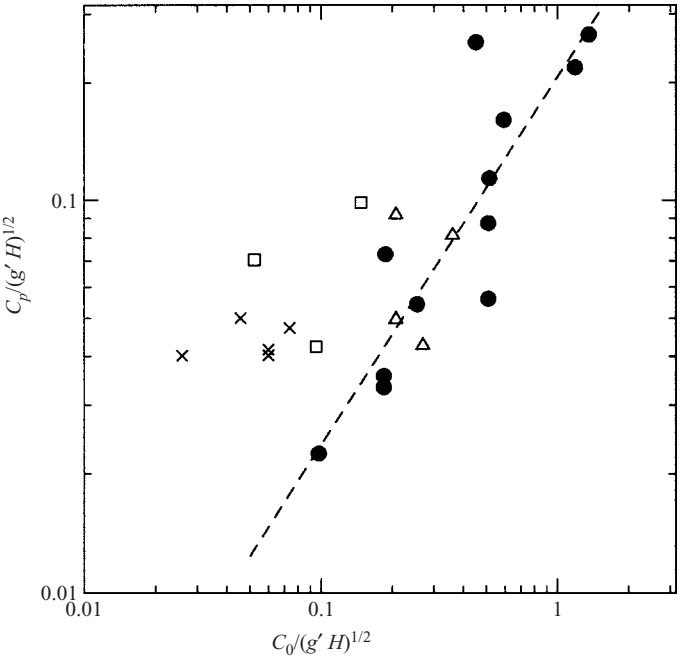

FIGURE 14. Phase speed of the unstable modes versus estimated upper-layer speed determined from PV conservation arguments. Symbols represent different ranges of σ, as in figure 12. The dashed line represents the best fit line through date with $\sigma < 8$ (solid circles).

of Taylor columns in this low Rossby number regime. The surface flow is found to be typically 10 to 50% faster than C_p in regions where the surface does not overlie the current or eddies.

Thus the instability of the current appears to be governed not by the baroclinic dynamics of the current but by the barotropic dynamics of the surface flow.

A crude theory allows us to estimate the characteristic azimuthal (linear) speed, C_0, of the surface flow. Ignoring the beta-plane dynamics induced by the slope, we compute the initial potential vorticity of the fluid directly over the annulus to be $Q_0 = f/H$. Now suppose the injected fluid compresses the upper layer to a depth of $H - D$. For conservation of potential vorticity, anticyclonic vorticity, $\zeta < 0$, must develop in the upper layer. Using the shallow water expression for potential vorticity, $Q = (f + \zeta)/(H - D)$, its conservation requires

$$\zeta = -\frac{fD}{H}. \tag{4.4}$$

Because this region of induced vorticity forms a current around a circle of radius R_0, we write $\zeta = 2(2\pi/T)$ where the period $T = 2\pi R_0/C_0$. Thus we predict

$$C_0 = -\frac{\Omega D R_0}{H}. \tag{4.5}$$

If the instability of the lower current is indeed controlled by barotropic instability of the surface flow, we expect that C_p should be proportional to C_0.

In figure 14 we plot C_p versus C_0, with both axes normalized by the shallow water speed based on the total fluid depth H. For relatively low-density currents, plotted with solid circles in the figure, the phase speed clearly increases with C_0. Indeed, a

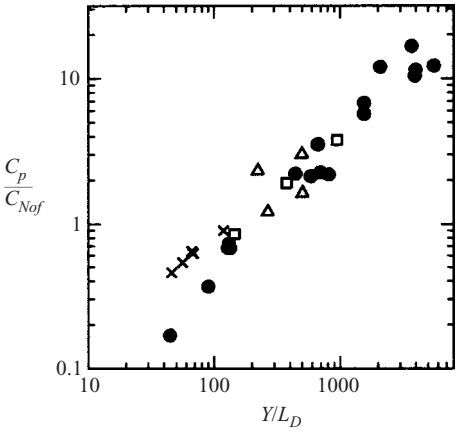

FIGURE 15. Ratio of phase to Nof speed versus ratio of Ekman pumping lengthscale, Y, to deformation radius L_D based on current depth. Different symbols are plotted depending on the relative density of the injected fluid as in figure 12.

best-fit line through these points gives a slope of 0.94 ± 0.08, which is consistent with the expected slope of 1. For currents with large densities, $\sigma > 64$, the phase speed is found to be approximately constant. For still larger σ, instability is suppressed in our experiments because the injected fluid pours downslope without building up into a domed current.

The transition to new, presumably baroclinically influenced dynamics occurs for $16 \lesssim \sigma \lesssim 64$. However, the non-barotropic behaviour of large-σ experiments is captured neither by (4.5) nor by existing baroclinic theories that neglect the induced motion of the ambient fluid (e.g. S91). Because the surface flow speed remains identical to the phase speed of the instability even at large σ, we primarily attribute the observed transition to density-influenced adjustments of our heuristically predicted value of C_0. Investigations into the governing dynamics are the subject of ongoing research.

Finally, we compare our experimental results with the eddy-speed criterion proposed by Lane-Serff & Baines (1998). On the basis of empirical evidence, they proposed that the ratio of the phase to Nof velocity should form a power law with the quantity Y/L_D. Here $L_D = (g'D)^{1/2}/f$ is the deformation radius based on the current depth, D, and $Y = Q/(C_{Nof}\delta)$ is an along-slope lengthscale based on the distance over which a volume flux Q propagating at the Nof speed, C_{Nof}, loses its fluid to Ekman pumping over a depth δ.

Figure 15 shows a log–log plot of C_p/C_{Nof} versus Y/L_D. Like the observations of Lane-Serff & Baines (1998), we find an excellent collapse of data. The best-fit line through the points gives the empirical prediction

$$\frac{C_p}{C_{Nof}} \simeq (0.17 \pm 0.01)\left(\frac{Y}{L_D}\right)^{0.80\pm0.11}. \tag{4.6}$$

In comparison, Lane-Serff & Baines (1998) found a power law exponent of 0.62 ± 0.06.

The approximate agreement between these two sets of experimental results is encouraging, particularly as the set-ups are different. Whereas we observe normal-mode instabilities in the form of temporally growing periodic disturbances on an axisymmetric current, Lane-Serff & Baines (1998) observe the sequential generation of eddies from a spatially localized source.

Despite the collapse of data in figure 15, it is not obvious how to interpret the dynamics underlying the resulting power law. For example, the lengthscale Y is defined under the assumption that eddies propagate at the Nof speed. However, the same plot shows that the observed phase speed varies by an order of magnitude about C_{Nof}.

To develop physical insight into the principles resulting in a power law, we take our empirically measured decimal exponent in (4.6) to be exactly 4/5 and we write C_{Nof}, Y and L_D explicitly in terms of measured quantities. Thus we find

$$C_p \propto C_{Nof}\left(\frac{Q}{C_{Nof}\delta L_D}\right)^{4/5} \propto (g')^{-1/5} D^{-2/5} f. \tag{4.7}$$

In (4.7), we have removed the explicit dependence on Q, s and ν since these are constant in all our experiments.

Equation (4.7) shows that C_p varies approximately linearly as f but varies as g' and D with small negative exponents. In particular, for values of D ranging from 2 to 7 in our experiments, the factor $D^{-2/5}$ changes by only 40%. Likewise a 32-fold increase in σ results only in halving of C_p.

Thus C_p is only weakly dependent upon g' and D, and even this predicted weak dependence reveals a discrepancy with data. Figure 15 shows that for fixed Y/L_D, C_p/C_{Nof} is larger in experiments with $\sigma > 64$ relative to experiments with $\sigma < 8$. The observed g' dependence in fact is not well captured by (4.7).

We conclude that the dominant factor determining collapse of the data in figure 15 is the linear dependence of C_p on f.

Indeed, this is exactly the dependence predicted by (4.5). Thus, whereas the plot in figure 15 reveals an empirically determined power law with ambiguous physical interpretation, we believe this occurs as a mathematical consequence of the approximate relation in (4.5) and the hypothesis that barotropic instability of the surface flow controls the dynamics of the dense current, at least in experiments with small σ.

5. Conclusions

We have constructed a novel experimental apparatus that allows us to examine bottom-dwelling dense axisymmetric currents without explicitly disturbing the surface as one would, for example, by rapidly extracting two concentric cylinders in a standard lock-release mechanism. The experiment is similar to those by Lane-Serff & Baines (1998), Etling *et al.* (2000), Cenedese *et al.* (2004) and others in that dense fluid is injected along the bottom of a sloping surface. Our set-up, in which fluid is injected around an annulus on a conical bottom, has the added advantage of establishing an axisymmetric initial condition similar to that of Choboter & Swaters (2000) except that we have a non-stationary ambient. This simple geometry more easily facilitates interpretation of our results.

Instability is observed in experiments with bottom flows that are sufficiently deep compared with the total fluid depth and sufficiently wide compared with the Rossby radius L_R. When unstable, the number of waves that develop around the annulus is between $N_\lambda = 3$ and 7. For the range of the interaction parameter, μ, to which our experiments correspond, the range of N_λ is much narrower than that predicted by the baroclinic stability theory of S91. Likewise, the ratio of the observed phase speed to Nof speed is found to vary greatly, contrary to S91. Whereas baroclinically unstable currents develop undulations on their downslope flank, we observe sinusoidal undulations extending across the width of the current.

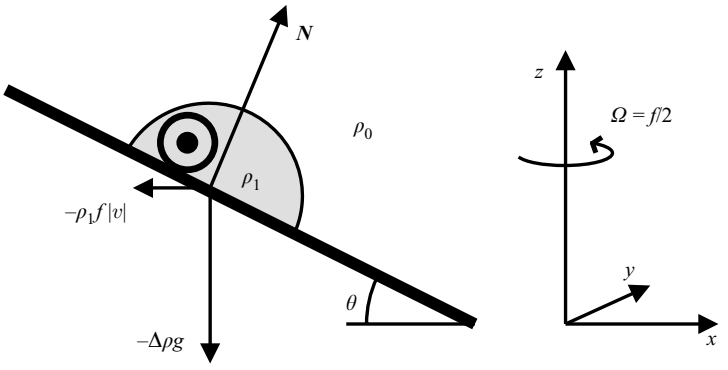

FIGURE 16. Schematic showing body forces acting on a geostrophically balanced current on a slope.

The discrepancy is not surprising, since S91 assumes the ambient fluid is stationary, which is clearly observed not to be the case in our experiments and, indeed, in most experiments on rotating gravity currents. Surface tracers reveal that the surface flow speed above the annulus is approximately equal to the phase speed of the instability, thus showing that the surface flow dynamics cannot be neglected when considering the evolution of dense eddies. (By analogy, if fluid was injected from the surface, this would induce a flow in the underlying ambient and one would expect the resulting instability to be qualitatively different from that described by Killworth, Paldor & Stern (1984) and Paldor & Killworth (1987), who likewise assumed a stationary ambient.) If the density of the bottom current is relatively small, the observed instability of the current is driven entirely by barotropic instability of the surface jet. For currents that are more dense ($\sigma \gtrsim 16$), the phase speed of the instability is moderately different from that predicted by the barotropic instability hypothesis.

At present, no theory exists that predicts the unstable characteristics of a dense current with an overlying non-stationary ambient. From ongoing research we will develop a better understanding of this system through analysis of numerical simulations that model the bottom injection of fluid. We will also examine the dynamics of a current injected from a semi-circular annulus, thus enabling us to connect our analysis here of temporally growing normal-mode instabilities to the analysis of spatially growing instabilities from localized, asymmetric disturbances. We will further examine the long-time, fully nonlinear evolution of the eddies in numerical and experimental circumstances.

The experiments were performed in the Environmental and Industrial Fluid Dynamics Laboratory at the University of Alberta. This work has been supported by funding from the Natural Sciences and Engineering Research Council of Canada Discovery Grants and USRA programs.

Appendix. Derivation of Nof velocity

Here we provide a simple derivation of the Nof velocity based on elementary physical arguments similar to the 'banking problem'. We imagine that fluid of density ρ_1 moves in geostrophic balance as shown in figure 16. Here the flow bounded by the slope on the west in a counterclockwise-rotating frame of reference. If the fluid moves

southward with speed $|v|$, Coriolis effects drive the current westward into the slope with force per unit mass of $F_x = -f|v|$. Meanwhile, buoyancy forces drive the current vertically downward with force per unit mass of $F_z = -g'$, in which $g' = g(\rho_1 - \rho_0)/\rho_1$ is the reduced gravity. Both these forces are balanced by a normal (body) force $\boldsymbol{N}$ acting normal to the slope.

Resolving the forces in the x- and z-directions and eliminating $|\boldsymbol{N}|$ gives $\tan\theta = f|v|/g'$.

Writing the slope $s = \tan\theta$ and solving for $|v|$ gives the Nof speed

$$C_{Nof} = \frac{sg'}{f}.$$

The derivation of this speed required the presence of a normal force $\boldsymbol{N}$. This demonstrates that the geostrophically balanced speed of the current is not determined solely by beta-plane dynamics: a surface current with an underlying slope behaves differently to a bottom current on the slope.

REFERENCES

Benjamin, T. B. 1968 Gravity currents and related phenomena. *J. Fluid Mech.* **31**, 209–248.

Cenedese, C., Whitehead, J. A., Ascarelli, T. A. & Ohiwa, M. 2004 A dense current flowing down a sloping bottom in a rotating fluid. *J. Phys. Oceanogr.* **34**, 188–203.

Choboter, P. & Swaters, G. E. 2000 On the baroclinic instability of axisymmetric rotating gravity currents with bottom slope. *J. Fluid Mech.* **408**, 149–177.

Dalziel, S. B. 1993 Rayleigh-Taylor instability: experiments with image analysis. *Dyn. Atmos. Oceans* **20**, 127–153.

Etling, D., Gelhardt, F., Schrader, U., Brennecke, F., Kühn, G., d'Hieres, G. C. & Didelle, H. 2000 Experiments with density currents on a sloping bottom in a rotating fluid. *Dyn. Atmos. Oceans* **31**, 139–164.

Griffiths, R. W., Killworth, P. D. & Stern, M. E. 1982 Ageostrophic instability of ocean currents. *J. Fluid Mech.* **117**, 343–377 (referred to herein as GKS 82).

Griffiths, R. W. & Linden, P. F. 1982 Laboratory experiments on fronts. *Geophys. Astrophys. Fluid Dyn.* **19**, 159–187.

Houghton, R. W., Schlitz, R., Beardsley, R. C., Butman, B. & Chamberlin, J. C. 1982 The middle Atlantic bight pool: Evolution of the temperature structure during 1979. *J. Phys. Oceanogr.* **12**, 1019–1029.

Jungclaus, J. H., Hauser, J. & Käse, R. H. 2001 Cyclogenesis in the denmark strait overflow plume. *J. Phys. Oceanogr.* **31**, 3214–3229.

Killworth, P. D., Paldor, N. & Stern, M. E. 1984 Wave propagation and growth on a surface front in a two-layer geostrophic current. *J. Mar. Res.* **42**, 761–785.

Lane-Serff, G. F. & Baines, P. G. 1998 Eddy formation by dense flows on slopes in a rotating fluid. *J. Fluid Mech.* **363**, 229–252.

Mellor, G. L. 1996 *Introduction to Physical Oceanography.* American Institute of Physics.

Mory, M., Stern, M. E. & Griffiths, R. W. 1987 Coherent baroclinic eddies on a sloping bottom. *J. Fluid. Mech.* **183**, 45–62.

Nof, D. 1983 The translation of isolated cold eddies on a sloping bottom. *Deep-Sea Res.* **30**, 171–182.

Paldor, N. & Killworth, P. D. 1987 Instabilities of a two-layer coupled front. *Deep-Sea Res.* **34**, 1525–1539.

Rottman, J. W. & Simpson, J. E. 1983 Gravity currents produced by instantaneous releases of a heavy fluid in a rectangular channel. *J. Fluid Mech.* **135**, 95–110.

Saunders, P. M. 1973 The instability of a baroclinic vortex. *J. Phys. Oceanogr.* **3**, 61–65.

Spall, M. A. & Price, J. F. 1998 Mesoscale variability in Denmark Strait: The PV outflow hypothesis. *J. Phys. Oceanogr.* **28**, 1598–1623.

Swaters, G. E. 1991 On the baroclinic instability of cold-core coupled density fronts on a sloping continental shelf. *J. Fluid Mech.* **224**, 361–382 (referred to herein as S91).

Swaters, G. E. & Flierl, G. R. 1991 Dynamics of ventilated coherent cold eddies on a sloping bottom. *J. Fluid Mech.* **223**, 565–587.

Whitehead, J. A., Stern, M. E., Flierl, G. R. & Klinger, B. A. 1990 Experimental observations of baroclinic eddies on a sloping bottom. *J. Geophys. Res.* **95**, 9585–9610.